ACS Catalysis

Research Article

Cite This: *ACS Catal.* 2019, 9, 5231−5244

pubs.acs.org/acscatalysis

Identification of a Pt_3Co Surface Intermetallic Alloy in Pt−Co Propane Dehydrogenation Catalysts

Laryssa Goncalves Cesar,[†] Ce Yang,[‡,§] Zheng Lu,[§] Yang Ren,[∥] Guanghui Zhang,*[,†,⊥] and Jeffrey T. Miller*[,†]

[†]Davidson School of Chemical Engineering, Purdue University, West Lafayette, Indiana 47907, United States
[‡]NOVA Chemicals Center for Applied Research, Calgary, Alberta T2E 7K7, Canada
[§]Chemical Sciences and Engineering Division, Argonne National Laboratory, Argonne, Illinois 60439, United States
[∥]X-Ray Science Division, Argonne National Laboratory, Argonne, Illinois 60439, United States
[⊥]State Key Laboratory of Fine Chemicals, PSU-DUT Joint Center for Energy Research, School of Chemical Engineering, Dalian University of Technology, Dalian, Liaoning 116024, People's Republic of China

ABSTRACT: Bimetallic Pt−Co nanoparticles (NPs) were prepared and characterized by scanning transmission electron microscopy, in situ X-ray absorption spectroscopy, in situ synchrotron X-ray diffraction, and catalytic conversion for propane dehydrogenation with and without added H_2. In addition, the surface extended X-ray absorption fine structure (EXAFS) obtained by fitting the difference spectrum between the fully reduced and room-temperature-oxidized catalysts suggest that the surface structure remains Pt_3Co, although the core changes from Pt to Pt_3Co and to PtCo. At low Co loading, the bimetallic nanoparticles form a Pt_3Co intermetallic surface alloy with Pt-rich core. With increasing Co loading, a full alloy forms where both the surface and NP compositions are Pt_3Co. A further increase in Co loading leads to a Co-rich NP core, likely PtCo, with a surface of Pt_3Co. Although Pt−Co intermetallic alloys form two different phases and several morphologies, the surface structures are similar in all catalysts. Although both monometallic Pt and Co are active for alkane dehydrogenation, all bimetallic Pt−Co catalysts are significantly more olefin selective than either single metal. The turnover rates of the bimetallic catalysts indicate that Pt is the active atom with little contribution from Co atoms. The high olefin selectivity is suggested to be due to Co acting as a less active structural promoter to break up large Pt ensembles in bimetallic NPs.

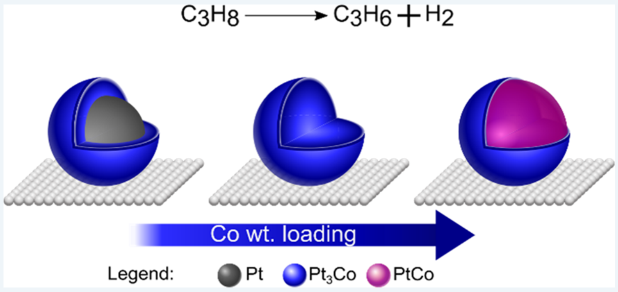

KEYWORDS: *alkane dehydrogenation, bimetallic Pt−Co catalysts, in situ EXAFS analysis of Pt−Co nanoparticles, synchrotron nanoparticle X-ray diffraction of Pt−Co nanoparticle, intermetallic Pt−Co alloy formation, bimetallic nanoparticle surface structure determination*

1. INTRODUCTION

In heterogeneous catalysts, chemical reactions occur at the interface between the gas-phase reactants and surface atoms. The reaction mechanisms happen through multiple steps involving reactant adsorption, adsorbate reaction, and the product desorption. The surface structure is, therefore, responsible for determining these reaction pathways, as it determines not only the reaction rates but also the selectivity toward certain products.

One important example is propane dehydrogenation, where C−H bonds (reaction I) are broken to form propylene. Since this reaction is highly endothermic, it requires high temperatures which also favor light gas formation by hydrogenolysis and rapid deactivation by coke formation. Hydrogenolysis reactions are due to C−C bond dissociation (reaction II) in the presence of H_2, while the coke formation on the surface rapidly deactivates the catalysts by active sites blockage. Active catalysts for propane dehydrogenation processes are those of group VIII metals such as Pt, Pd, Co, and Fe.[1] Among these, Pt shows the highest activity, at temperatures as low as 500 °C, and the best olefin selectivity due to its superior ability to favor reaction I over reaction II. However, its reported olefin selectivity is still low, typically about 60−80%.[2−5]

$$C_3H_8 \leftrightarrow C_3H_6 + H_2 \qquad \text{(I)}$$

$$C_3H_8 + H_2 \leftrightarrow C_2H_6 + CH_4 \qquad \text{(II)}$$

Reduction of hydrogenolysis rate improves propylene selectivity and can be achieved by adding nonactive, post-transition metals as promoters forming bimetallic Pt catalysts. Sn is the most common promoter, being commercially available, with a reported selectivity ranging from 74% to 96%.[4−11]

Received: February 5, 2019
Revised: April 11, 2019
Published: April 24, 2019

DOI: 10.1021/acscatal.9b00549
ACS Catal. 2019, 9, 5231−5244

Reported catalysts for light alkane dehydrogenation often contain Pd or Pt as the active metal and a second metal as a promoter, such as Pd−Zn, Pt−Ga, Pt−Ge, Pt−Pb, Pt−Cu, Pd−In, Pt−In, and Pt−Sb, with an initial selectivity above 90%.[12−20] This increase in selectivity can be attributed to the inhibition of hydrogenolysis and coke formation. According to Boudart, catalyzed reactions can be classified as structure sensitive and structure insensitive.[21,22] Hydrogenolysis, being an example of the former, is affected by the surface ensemble size, while dehydrogenation is a structure-insensitive reaction where all surface Pt atoms are active.[23−25] The addition of a noncatalytic promoter acts by decreasing the surface Pt ensemble size, responsible for hydrogenolysis. The high selectivity of bimetallic Pt NPs is, therefore, linked to the geometric effect caused by the noncatalytic promoter.[2,12] Bimetallic NPs can form either a solid solution (disordered structure) or an intermetallic compound (ordered structure). Common ordered alloy phases are Pt_3M[18] and PtM,[12,19] with Au_3Cu and AuCu structures, respectively, as shown in Figure 1. Both structures have fewer Pt−Pt neighbors, resulting in small Pt ensembles or isolated Pt atoms.

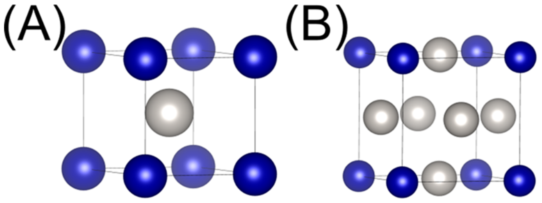

Figure 1. Schematics for (a) a PtM (AuCu type) and (b) Pt_3M (Au_3Cu) alloy phase structures. The Pt atoms are represented in gray and promoter atoms in blue.

In addition to single-phase bimetallic and alloy phases, the nanoparticles can also form two phases: for example, a bimetallic shell with a monometallic Pt core.[18,26,27] In such cases, it is crucial to determine the surface composition to understand the reaction selectivity. However, in small nanoparticles (<2 nm), this can be challenging due to the limitations of traditional surface analysis methods, especially when two phases are present.

Cobalt forms two ordered intermetallic compounds with Pt, Pt_3Co and PtCo.[28] Given that Co is also a VIII group metal, it is also active for propane dehydrogenation but exhibits a poor selectivity and rapid deactivation in comparison to Pt.[1] Therefore, it might be expected that promoting Pt with Co might result in a catalyst with poor selectivity and stability from the Pt−Co ensembles. Additionally, PtCo alloys have been reported to improve activity in electrocatalysts, but careful characterization to differentiate solid solutions and intermetallic compounds has not been performed.[29,30]

The goal of this work is to synthesize and investigate the surface structure of bimetallic Pt−Co catalysts for propane dehydrogenation where two intermetallic compounds are formed, PtCo and Pt_3Co. The catalysts were prepared, and their catalytic performance for propane dehydrogenation was determined. Additionally, their structures were determined by in situ X-ray absorption spectroscopy (XAS), synchrotron X-ray diffraction (XRD), and surface extended X-ray absorption fine structure (EXAFS) analysis.

2. EXPERIMENTAL SECTION

2.1. Catalyst Synthesis. A series of catalysts were synthesized using a fixed amount of Pt (2 wt %) with varying weight loadings of Co: 2 wt % Pt−0.6 wt % Co (2Pt0.6Co), 2 wt % Pt−1 wt % Co (2Pt1Co), 2 wt % Pt−2 wt % Co (2Pt2Co), and 2 wt % Pt−4 wt % Co (2Pt4Co). Monometallic Pt and Co catalysts were also prepared for comparison. All catalysts were supported on SiO_2 (Davisil 636 silica gel, Sigma−Aldrich, 35−60 mesh, surface area 480 m^2/g, pore volume 0.75 cm^3/g).

For the monometallic catalysts, a 3 wt % Pt ($3Pt/SiO_2$) and a 10 wt % Co ($10Co/SiO_2$) catalyst were prepared by incipient wetness impregnation (IWI), while a 2 wt %, single-site Co^{II}/SiO_2 was prepared by strong electrostatic adsorption (SEA).[31]

For the 3 wt % Pt catalyst, the precursor solution was prepared by dissolving 0.3 g of tetraamineplatinum(II) nitrate ($Pt(NH_3)_4(NO_3)_2$, Sigma-Aldrich) in 5 mL of a solution of deionized water and NH_4OH. The NH_4OH was added for pH correction to about 11. This solution was then added dropwise to 5 g of dry SiO_2 until the SiO_2 was moist to avoid overimpregnation of the pores. This method is called charge enhanced dry impregnation (CEDI).[31] The impregnated SiO_2 was then dried overnight at 125 °C, followed by calcination at 350 °C for 3 h. The reduction step was performed under a 5% H_2/95% N_2 atmosphere at 250 °C for 30 min, followed by 600 °C for another 30 min.

Similarly, the metallic Co/SiO_2 was prepared by two sequential impregnations of cobalt(II) nitrate hexahydrate ($Co(NO_3)_2{\cdot}6H_2O$, Sigma-Aldrich). Initially, 3.7 g of cobalt nitrate was dissolved in 15 mL of deionized water and the solution was mixed with 15 g of dry SiO_2 by dropwise addition. This yielded a total 5 wt % Co loading to the catalyst. During this preparation, the pH was not adjusted with NH_4OH to avoid precipitation of the precursor. After impregnation, the catalyst was dried overnight at 125 °C, followed by calcination at 400 °C for 3 h. The calcined catalyst went through a second impregnation using the same amount of precursor solution and the same conditions for the drying and calcination steps. To fully reduce the Co precursor, the catalyst was reduced in 5% H_2/95% N_2 at 750 °C for 30 min.

For the single-site Co^{II}/SiO_2, the synthesis occurred through strong electrostatic absorption (SEA) with hexamine cobalt(III) chloride ($Co(NH_3)_6Cl_3$, Sigma-Aldrich) as a precursor, as described by Hu et al.[32] The precursor solution was prepared by dissolving 1.7 g of $Co(NH_3)_6Cl_3$ in about 50 mL of deionized water and NH_4OH, to adjust the pH to 11. Simultaneously, 15 g of SiO_2 was suspended in 50 mL of H_2O in a separate beaker, also correcting the pH to 11 by NH_4OH. This pH deprotonates the surface SiOH and results in a negatively charged surface, allowing the metal cations to be strongly adsorbed to the support. The precursor solution was mixed with the SiO_2 and stirred for 20 min to allow the adsorption and saturation of the metal cation on the support surface. After the SiO_2 settled, the solids were separated by decantation and triple-rinsed with deionized water and vacuum-filtered. The filtered solids were dried first at room temperature and then at 125 °C, both for overnight periods. Finally, the catalyst was calcined at 400 °C for 3 h.

For the lowest Co loading, 2Pt0.6Co, the chosen method was also CEDI. The precursor solution was prepared for a total volume of 4.5 mL, containing 0.2 g of $Pt(NH_3)_4(NO_3)_2$ and 0.136 g of $Co(NH_3)_6Cl_3$, with pH correction to 11 with NH_4OH. This solution was added dropwise to 5 g of dry SiO_2,

DOI: 10.1021/acscatal.9b00549
ACS Catal. 2019, 9, 5231−5244

and the resulting catalysts were sequentially dried at room temperature and 125 °C, for overnight periods, and then calcined at 225 °C for 3 h.

For the 2Pt1Co on SiO_2, a precursor solution of 1 wt % Co was initially prepared for SEA, similarly to the Co^{II} single site method. A 15 mL solution containing 0.227 g of $Co(NH_3)_6Cl_3$ was added to 5.0 g of a SiO_2 suspension in 25 mL of water, both at pH 11, and the mixture was stirred for 20 min. After the solids settled, they were triple-rinsed, vacuum-filtered, dried at room temperature and 125 °C for overnight periods, and calcined at 400 °C for 3 h. The resulting solid had 1 wt % Co loading, and it was then impregnated (CEDI) with 4.5 mL of a precursor Pt solution at a pH of 11 with NH_4OH, containing 0.2 g of $Pt(NH_3)_4(NO_3)_2$, by dropwise addition. This resulting solid was dried as described previously and calcined at 225 °C for 3 h.

The procedure for the $2Pt2Co/SiO_2$ catalyst was the same as described for 2Pt1Co, via initial SEA and followed by IWI with Pt. The precursor solution for SEA contained 0.567 g of $Co(NH_3)_6Cl_3$ for the same 15 mL volume to reach a 2 wt % Co loading on the catalyst. The precursor solution for IWI contained the same amount of Pt. The synthesis, drying, and calcination procedures were performed as described above.

For 2Pt4Co, the initial step was also SEA to produce an initial 3 wt % Co/SiO_2 catalyst. A 25 mL portion of precursor solution was prepared with 1.114 g of $Co(NH_3)_6Cl_3$, and it was stirred with 5.0 g of suspended SiO_2 in 25 mL of deionized water for 20 min, with the system kept at pH 11. Similarly to the previous catalysts, the solids were rinsed, vacuum-filtered, dried, and calcined at 400 °C for 3 h. The resulting catalyst was then impregnated with a Pt and Co precursor solution (CEDI) by dropwise addition. This solution contained 0.2 g of $Pt(NH_3)_4(NO_3)_2$ and 0.227 g of $Co(NH_3)_6Cl_3$ with the pH adjusted to 11, with a total volume of 5 mL. The catalysts were then dried as described before and calcined at 225 °C for 3 h.

After the last calcination, all of the bimetallic catalysts were reduced in flowing 5% H_2/95% N_2 sequentially at 250 °C and at 600 °C, both for 30 min.

2.2. Scanning Transmission Electron Microscopy (STEM).

STEM images were obtained at Argonne National Laboratory (ANL) to measure the particle size distribution. The images were analyzed using ImageJ software.[33] Depending on the catalysts, about 5−10 micrographs were taken at different places on the SiO_2 surface. In each image, it was possible to count about 50−100 particles. Therefore, the particle size distribution was determined using a sample space consisting of 200−400 particles for accurate determination of the mean particle size of the bimetallic catalysts.

2.3. Synchrotron X-ray Absorption Spectroscopy (XAS).

The X-ray absorption spectroscopy (XAS) characterization was carried out in the 10-BM bending magnet and 10-ID Insertion device beamlines, at the Advanced Photon Source facility at Argonne National Laboratory. The monochromator was calibrated by acquiring a metal foil spectrum at each absorption edge. A simultaneous measurement of the metal foil in a third chamber was performed for each catalyst for energy calibration. The spectra were obtained in situ in transmission mode for the Pt L_{III} edge and Co K edge in step scan mode in approximately 10 min. Before each measurement, the samples were reduced at 550 °C for 30 min under a 100 cm^3/min flow rate of 3.5% H_2 in balance He. The XAS cell was purged in He, and the measurements were taken at room temperature in the presence of He. He was purified with an Oxytrap to prevent oxidation of the reduced catalysts by trace O_2.

All of the acquired XAS data were fit using the WINXAS 3.1 software.[34] The EXAFS coordination parameters can be obtained by fitting the Fourier transform. The k^2-weighted Fourier transform magnitudes were fit for the coordination shell for the corresponding k space in the range $\Delta k = 2.6-12.1$ Å^{-1} by least-squares methods. The first shell was fit (magnitude and imaginary parts) in the range $R = 1.6-3.0$ Å. The Pt−Pt, Co−Co and Co−O experimental phases and amplitudes were determined from the Pt foil (12 Pt−Pt at 2.77 Å), Co foil (12 Co−Co at 2.51 Å) and CoO reference (6 Co−O at 2.13 Å), respectively.[35]

Additional experiments were performed at the Pt L_{III} edge for surface characterization in each bimetallic Pt−Co catalyst. After full reduction and data collection of the reduced catalysts, the catalysts were oxidized by air (20% O_2 in balance He) at room temperature for 30 min. A second scan was obtained on the surface-oxidized catalyst. To quantify the fraction of surface Pt, the XAS spectra were analyzed for both XANES and EXAFS. For the XANES, the oxidized spectra were fit through a linear combination between the fully reduced catalyst and a reference PtO spectrum: i.e., fully oxidized Pt^{II} prepared from oxidation of a 1 nm Pt/SiO_2 catalyst (the EXAFS contained four Pt−O bonds at 2.04 Å with no detectable Pt−Pt bonds). For the EXAFS determination of the surface Pt and Co composition, a difference spectra analysis was performed. The ψ spectrum for the oxidized catalyst was subtracted from that of the fully reduced catalyst. The result was a difference spectrum that represents the metal peaks (with a normal phase shift) at the catalyst surface. In addition, the difference spectrum has a negative a Pt−O peak: i.e., the phase is π radius out of phase in comparison to a standard Pt−O scattering pair. The surface Pt fraction can be obtained from the surface Pt−O CN. Fully oxidized PtO has a Pt−O coordination number equal to 4; therefore, the surface Pt−O CN/4 is equal to the fraction of surface Pt, i.e., the Pt dispersion.

2.4. Synchrotron X-ray Diffraction (XRD).

The XRD measurements were performed at the 11-ID-C beamline at the Advanced Photon Source at Argonne National Laboratory. This high-flux beamline provided high-energy X-rays at 105.70 keV (λ = 0.1173 Å) and featured a PerkinElmer large area detector.

Two in situ measurements were performed. The first diffraction pattern was collected after the samples were reduced at 600 °C, under a flow of 3.5% H_2 in balance He. The second measurement was taken postreduction at room temperature under the same 3.5% H_2 in balance He flow rate. Additional measurements of the empty cell and the SiO_2 support were taken under the same conditions for background subtraction.

The data were treated by using two software packages: Fit2D[36] and Materials Analysis Using Diffraction (MAUD).[37] The Fit2D program was used to calibrate and integrate the diffraction patterns, generating the 1D diffraction pattern of the intensity versus 2θ degrees. MAUD was used to simulate the diffraction patterns of the alloy phases from the literature structures. The alloy phase for each sample was determined by comparing the experimental and calculated patterns. For the monometallic catalysts, Pt and Co, the particle size could be estimated through a Scherrer equation calculation, where the full width at half-maximum (fwhm) values of the largest peaks were measured.

2.5. Catalyst Evaluation for Propane Dehydrogenation.

An appropriate amount of monometallic Pt/SiO_2 or the bimetallic $Pt-Co/SiO_2$ was mixed with SiO_2, totaling 1.0 g of catalyst bed, was loaded into a 1/2 in. o.d. quartz plug flow reactor, secured by quartz wool plugs. Each catalyst was reduced for 60 min in 5% H_2/95% N_2 at 50 cm^3/min at 550 °C before each test. Due to different activities between the catalysts, the amount of each Pt−Co/SiO_2 varied between 0.01 and 0.07 g. Different amount of catalysts were evaluated for initial conversions and selectivities (zero time on stream), corresponding to minimum catalyst deactivation. The gas products were detected by a gas chromatograph (GC; Agilent 6890) coupled to a FID detector. In a nonoxidative propane dehydrogenation reaction, only light hydrocarbons were detected: methane, ethane, ethylene, propane, and propylene. The conversion (X) was calculated by the propane molar difference between the inlet and outlet, while the propylene selectivity (S) was calculated on the basis of the gas product distribution. The formulas are shown below.

$$X = \frac{\text{moles of propane in inlet} - \text{moles of propane in outlet}}{\text{moles of propane in inlet}} \times 100\%$$

$$S = \frac{\text{moles of } C_3H_6}{\text{moles of } C_3H_6 + \frac{2 \times \text{moles of } C_2}{3} + \frac{\text{moles of } CH_4}{3}} \times 100\%$$

Two experimental conditions were tested: with and without cofeeding H_2. For the first screening, the total flow rate was 200 cm^3/min, with 2.5% C_3H_8 in balance N_2. For the H_2 cofeeding the total flow rate was 250 cm^3/min, with 2.0% C_3H_8 and 1.0% H_2 in balance N_2. Both experiments were at 550 °C and atmospheric pressure. Each run was performed for 45 min, with data points analyzed every 5 min. Due to coke formation, part of the converted propane stays on the surface, blocking some active sites and deactivating the catalysts. Thus, the initial conversion and selectivity were determined by extrapolation to zero deactivation at time t = 0 min, to minimize the effects of coke formation and to assume a clean surface for the catalysts for TOR estimations. The initial conversions were between 5 and 35%.

The monometallic Co/SiO_2 and single-site Co^{II}/SiO_2 were also tested. However, due to the very rapid deactivation and lower rates in comparison to the bimetallic Pt−Co, lower flow rates and larger amounts of catalysts were used.

3. RESULTS

3.1. Scanning Transmission Electron Microscopy. The nanoparticle size was determined by STEM. For an accurate representation, several images were taken at different spots on the SiO_2 surface and the mean particle size and deviation were obtained on the basis of the frequency distribution between 200 and 400 nanoparticles for each catalyst. Table 1 summarizes these results, and the 2Pt1Co and 2Pt4Co catalysts are shown in Figures 2 and 3, respectively.

Table 1. Particle Size Distribution of the Nanoparticles

catalyst	mean particle size (nm)	standard deviation (nm)
3Pt	2.3	0.6
10Co	12.4	4.6
2Pt0.6Co	1.3	0.1
2Pt1Co	1.6	0.4
2Pt2Co	1.8	0.1
2Pt4Co	1.4	0.4

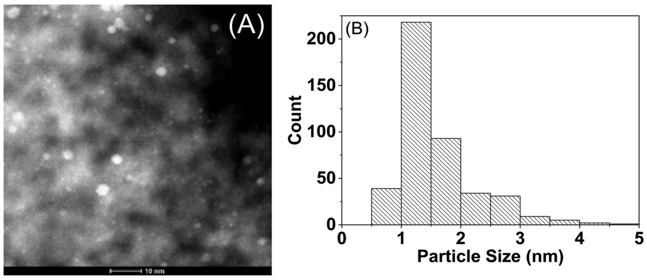

Figure 2. STEM images for (A) 2Pt1Co and (B) its respective particle size distribution.

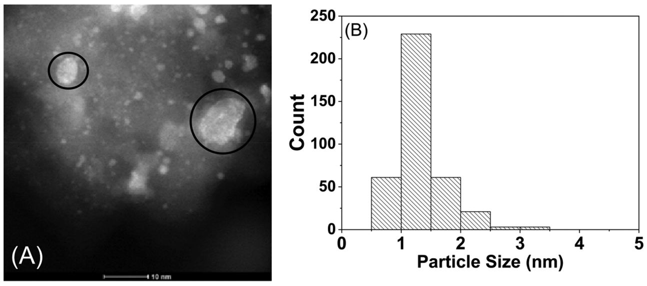

Figure 3. STEM images for (A) 2Pt4Co and (B) its respective particle size distribution. Large nanoparticles, likely monometallic Co, are circled in black.

The metallic Pt nanoparticles were found to be around 2.3 nm, while the 10Co nanoparticles were significantly larger at around 12 nm. For all of the bimetallic catalysts, the mean particle size distributions are similar, around 1.5 nm with few larger particles. The particles are also well distributed over the SiO_2 surface. At higher Co loading, 2Pt4Co, large nanoparticles of 10−20 nm are present, circled in black in Figure 3, along with well-dispersed small particles. It will be shown later by XRD that the former are likely monometallic Co. Single-site Co^{II}/SiO_2 showed no evidence of metallic Co or oxide NPs.

3.2. X-ray Absorption Spectroscopy (XAS). *3.2.1. Pt L_{III} Edge.* The XAS measurements for the bimetallic catalysts were performed at both the Pt L_{III} edge (11.564 keV) and Co K edge (7.709 keV). All measurements were taken at room temperature under a He atmosphere after reduction at 550 °C. The XANES spectra provide information regarding the oxidation state, while the EXAFS spectra identify the local coordination environment, such as bond distance and coordination number. The XANES spectra at the Pt L_{III} edge for the monometallic Pt and the bimetallic Pt−Co catalysts are shown in Figure 4. The monometallic Pt nanoparticles (NPs) have a shape, white line intensity, and edge energy (11.5640 keV) similar to those of a Pt foil (Table 2). The similarity to both the Pt foil and edge energy suggests that all the Pt atoms in this catalyst are fully reduced, with Pt atoms surrounded only by other Pt atom neighbors.

The 2Pt0.6Co spectrum shows a shape and white line intensity similar to those of the Pt NPs, with a slight shift to higher energy, implying that all the Pt atoms are fully reduced and the coordination environment is mainly neighboring Pt atoms. However, the slight decrease and broadening in the white line and the shift to higher edge energy, 11.5642 keV (Table 2), suggest the presence of neighboring Co atoms within bonding distance. In the 2Pt1Co spectrum, there is also a decrease in the white line intensity and a shift to higher edge energy. Its edge energy, 11.5647 keV (Table 2), is larger than that in 2Pt0.6Co, also suggesting higher levels of Co within the Pt bonding

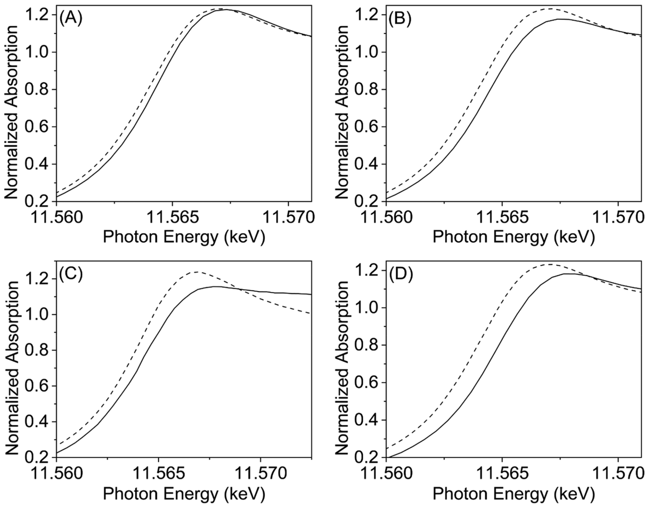

Figure 4. Comparison of the XANES spectra at the Pt L_{III} edge of 3Pt/SiO_2 (dashed line in all the figures) with those of (A) 2Pt0.6Co (solid line), (B) 2Pt1Co (solid line), (C) 2Pt2Co (solid line), and (D) 2Pt4Co (solid line).

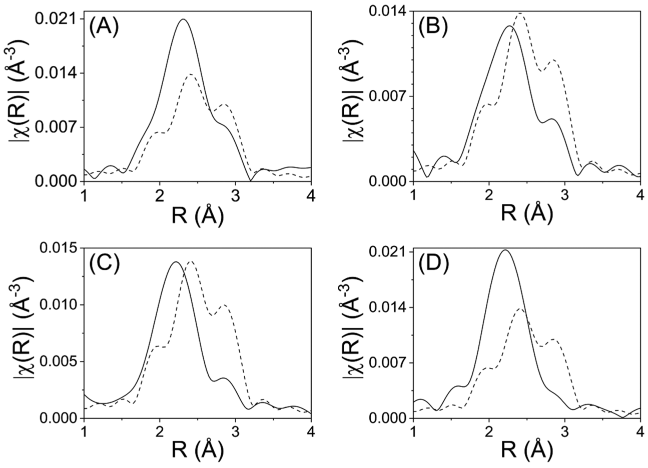

Figure 5. Comparison of the EXAFS spectra of 3Pt/SiO_2 (dashed line) at the Pt L_{III} edge with those of (A) 2Pt0.6Co (solid line), (B) 2Pt1Co (solid line), (C) 2Pt2Co (solid line), and (D) 2Pt4Co on the bottom (solid line).

distance. The Pt XANES spectrum of 2Pt2Co further decreases in white line intensity and shifts to higher edge energy, 11.5644 keV. Similarly, the 2Pt4Co XANES spectrum shifts even further (Table 2), indicative of bimetallic particles with an increasing Co composition.

The k^2-weighted magnitudes of the Fourier transform (FT) of the EXAFS spectra at the Pt L_{III} edge show different shapes among the four bimetallic particles and Pt (Figure 5). The imaginary parts of the FT (not shown) are also different for each catalyst. As shown in the monometallic Pt nanoparticle in Figure 5, Pt−Pt bonds show three peaks between 2 and 3 Å (phase uncorrected distance), where the center peak is the largest and the first peak is the smallest. By using the experimental phase and amplitude calculated for a Pt foil, the Pt/SiO_2 catalyst was fit. The Pt−Pt coordination number (CN) was 9.3 at 2.75 Å (Table 2). In a Pt foil, the Pt−Pt bond CN is 12 at 2.77 Å. These slightly shorter Pt−Pt bond distances are consistent with small Pt nanoparticles.[38]

The shape of the EXAFS spectrum of 2Pt0.6Co particles is strongly distorted in comparison to that of monometallic Pt (Figure 5A). The central peak is shifted to lower *R*, and the first and second peaks overlap. The third peak decreased sharply in intensity. The EXAFS spectrum was fit with an experimental Pt−Pt reference and FEFF6 simulated Pt−Co scattering pair. Good fits were obtained with a Pt−Pt bond length of 2.73 Å, with a CN of 7.9 and Pt−Co bond length of 2.56 Å with 2.5 CN. The EXAFS spectrum is consistent with the XANES spectrum and confirms the formation of bimetallic Pt−Co NPs. The higher Pt−Pt CN indicates that these particles are Pt-rich.

In the 2Pt1Co spectrum (Figure 5B), the central peak shifts to an even lower *R* value, overlapping with the first peak. The third (high *R*) peak is still present, but at a significantly lower height. A fit of the EXAFS spectrum gives a Pt−Pt CN of 4.5 at 2.73 Å and a Pt−Co CN of 2.2 at 2.56 Å (Table 2). The bimetallic NPs are also Pt-rich but contain more Co than in the 2Pt0.6Co, consistent with the larger shift in the XANES energy. The (Pt−Co):(Pt−Pt) CN ratio is about 1:2 in the reduced catalyst.

The 2Pt2Co catalyst spectrum, as shown in Figure 5c and Table 2, has a similar shape to that of 2Pt1Co, with the first and central peak overlapping but with an even lower height third peak. The fit has a Pt−Pt CN of 3.0 at 2.73 Å and a Pt−Co CN of 2.9 at 2.56 Å. The (Pt−Co):(Pt−Pt) ratio CN ratio was about 1:1. Thus, these bimetallic NPs contain about equal amounts of Pt and Co and an increased Co composition in comparison to 2Pt1Co.

In the 2Pt4Co spectrum, only one large peak shifted to low *R* is present. Due to the large number of Pt−Co bonds, it is difficult to quantify the Pt−Pt CN in the first shell. As a result, the Pt−Pt bond distance for the shell was fixed at 2.73 Å, similarly to those in the other catalysts. The resulting Pt−Co bond distance is 2.55 Å with a CN of 5.2, while Pt−Pt has a CN of 2.5 at 2.73 Å (Table 2). The (Pt−Co):(Pt−Pt) CN ratio was approximately 2:1. These NPs have the highest Co content of the four bimetallic catalysts.

Table 2. EXAFS Data at the Pt L_{III} Edge for the Fully Reduced Bimetallic Pt−Co and Monometallic Pt Catalysts

catalyst	edge energy (keV)	bond	bond length (Å)	CN	(Pt−Co):(Pt−Pt)	σ^2	E_0 shift (eV)
3Pt	11.5640	Pt−Pt	2.75	9.3	0	0.002	−1.1
2Pt0.6Co	11.5642	Pt−Pt	2.73	7.8	0.32	0.002	0.22
		Pt−Co	2.56	2.5		0.002	−1.89
2Pt1Co	11.5647	Pt−Pt	2.73	4.5	0.49	0.002	−1.31
		Pt−Co	2.56	2.2		0.002	1.05
2Pt2Co	11.5644	Pt−Pt	2.73	3.0	0.97	0.002	−2.21
		Pt−Co	2.56	2.9		0.002	3.23
2Pt4Co	11.5645	Pt−Pt	2.73	2.5	2.08	0.002	−3.48
		Pt−Co	2.56	5.2		0.002	4.64

The Pt L_{III} EXAFS spectra show the same trends observed with the XANES spectra. As the Co metallic loading increases, bimetallic particles are formed with increasing amounts of Co in the metallic NPs.

3.2.2. Co K Edge. The XANES spectra at the Co K edge of the bimetallic Pt−Co, monometallic Co, and single-site Co^{II}/SiO_2 catalysts are shown in Figure 6. The shape of the spectra and the edge energy of the monometallic $10Co/SiO_2$ (7.709 keV) are similar to those of the Co foil (Figure 6 (dotted lines) and Table 2), suggesting that $10Co/SiO_2$ is fully reduced.

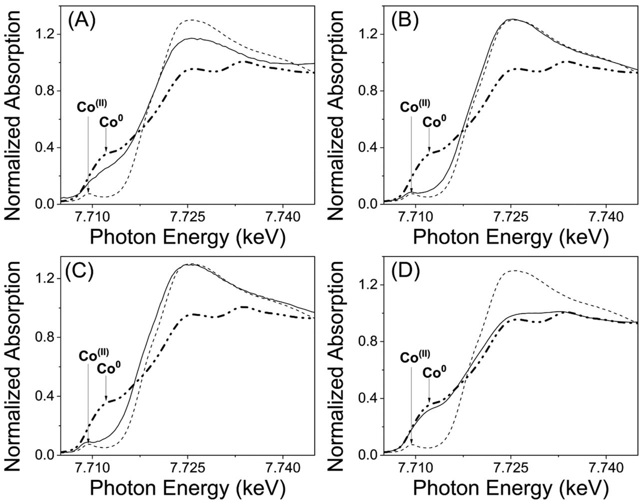

Figure 6. Comparison of XANES spectra at the Co K edge between metallic Co (bold dashed-dotted line) and Co^{II} (dashed line) oxidation states with (A) 2Pt0.6Co (solid line), (B) 2Pt1Co (solid line), (C) 2Pt1Co (solid line), and (D) 2Pt4Co (solid line).

The XANES spectrum for $2Co^{II}/SiO_2$ (Figure 6 (dashed lines)), on the other hand, shows a large white line intensity, as well as a higher XANES edge energy. The pre-edge peak at 7.7085 keV is consistent with a Co^{2+} oxidation state.[32]

The spectrum for 2Pt0.6Co has an intermediate shape in comparison to monometallic Co and Co^{II}. Both the edge energy, 7.7202 keV (Table 2), and the larger white line are similar to those expected for Co^{II}. A linear combination (LC) fit using the monometallic Co^0 and Co^{II} single-site spectra suggests the fraction of Co^{II} is 0.41, while the remaining 0.59 is metallic Co (Table 3). Therefore, at 0.6% Co loading, not all Co atoms have been fully reduced and alloyed with Pt. There is a significant fraction of unreduced Co^{II}.

The spectrum for 2Pt1Co is similar to that of Co^{II}, except for a slight increase in absorption between the pre-edge peak and the white line, suggesting that almost all the Co is present as Co^{II} ions. The edge energy is, at 7.7173 keV (Table 2), slightly lower than the expected energy for pure Co^{II} species. The LC fit suggests that the Co^{II} single-site fraction is 0.89 while the remaining 0.11 is metallic. Given the previous results in the Pt L_{III} edge, it is likely that the metallic Co is present in the Pt−Co bimetallic NPs (Table 3). The larger fraction of Co^{II} likely results from the higher Co loading. Similarly, the XANES spectrum for the 2Pt2Co catalysts gives a LC fit with a Co^{II} fraction of 0.79, indicating a large fraction of unreduced Co^{II}.

The spectrum of 2Pt4Co is similar in shape to that of the monometallic Co. This catalyst has a slight decrease in the absorption edge around 7.7110 keV, with a slightly higher white line in comparison to Co^0. Its edge energy, however, is 7.7089 keV (Table 2), the same as in the monometallic Co spectra. The LC fit suggests that the fraction of Co^{II} is 0.14, while the remaining 0.86 is reduced (Table 3).

Figure 7 shows the Fourier transform (FT) of the EXAFS spectra for the Co foil, $2Co^{II}/SiO_2$, and bimetallic Pt−Co particles. As shown in Figure 7D, Co foil, i.e., metallic Co, has a first shell around 2 Å (phase uncorrected distance) consisting of one large peak with a small shoulder at lower R. From the EXAFS fit, the Co−Co bonds in $10Co/SiO_2$ have an average distance of 2.52 Å with a CN of 12 (Table 2), suggesting a large size for these nanoparticles.

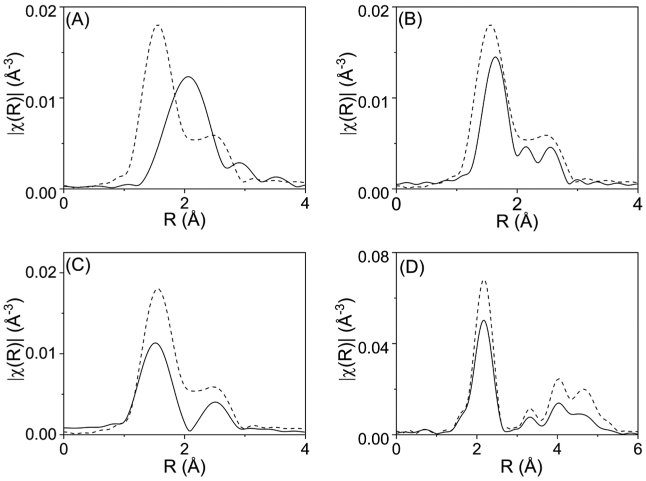

Figure 7. FT magnitudes of EXAFS spectra at the Co K edge: (A) comparison of 2Pt0.6Co (solid line) and Co^{II} peaks (dashed line); (B) comparison between 2Pt1Co (solid line) and Co^{II} peaks (dashed line); (C) comparison between 2Pt2Co (solid line) and Co^{II} peaks (dashed line); (D) comparison between 2Pt4Co (solid line) and Co foil (dashed line).

The $2Co^{II}/SiO_2$ spectrum, on the other hand, has a characteristic peak at lower R (about 1.5 Å phase uncorrected distance) and negligible peaks at higher R. The EXAFS can be fit with 4.2 Co−O bonds at 1.98 Å and is consistent with Co^{II} single sites on SiO_2 previously reported,[32] and no bulk Co oxides are visible.

Table 3. XANES and EXAFS Dta at the Co K Edge for the Fully Reduced Pt−Co Bimetallic and Monometallic Co Catalysts

catalyst	edge energy (keV)	Co^0 fraction	Co^{2+} fraction	bond	bond distance (Å)	CN	σ^2	E_0 shift (eV)
10Co	7.7090	1.00		Co−Co	2.52	12	0.002	−0.2
$2Co^{II}$	7.7176		1.00	Co−O	1.98	4.2	0.000	−1.0
2Pt0.6Co	7.7202	0.59	0.41					
2Pt1Co	7.7173	0.11	0.89					
2Pt2Co	7.7166	0.21	0.79					
2Pt4Co	7.7089	0.86	0.14	Co−Co	2.51	11.4	0.002	−0.8

The EXAFS spectra at the Co K edge for the reduced bimetallic samples are shown in Figure 7. Due to the overlapping Co−Co, Co−Pt, and Co−O peaks in 2Pt0.6Co and 2Pt1Co, it is not possible to obtain a satisfactory fit of these spectra. A qualitative analysis, however, confirms what was observed in XANES. In the spectrum of 2Pt0.6Co, the main peak matches the position for the metallic Co peaks with some residual Co−O bonds. This is consistent with the 0.59 metallic Co fraction found in XANES. The spectrum of 2Pt1Co matches the peak position for Co^{II}, also consistent with the 0.89 fraction found in XANES.

In the Co K edge EXAFS, 2Pt4Co has the same shape as the monometallic Co particles, with slightly lower magnitude of the Fourier transform. An even higher shell scattering, between 3 and 5 Å (phase uncorrected distance), can be observed, suggesting the presence of fully reduced but larger monometallic Co nanoparticles with an hcp structure. These Co−Co bond lengths are 2.50 Å with a CN of 11.4 (Table 2), consistent with the XANES LC fit. Given the strong presence of monometallic Co and the small fraction of Co^{II}, Pt−Co and Co−O bonds are not observed.

The trend in the EXAFS spectra is consistent with that of the XANES spectra. Despite formation of bimetallic Pt−Co particles, there is an excess of Co^{II} single sites on the surface for loadings less than 2%. As the Co loading increases, the available amount of Co^{II} single-site species increases until enough Co^{II} species are available to fully reduce into metallic Co nanoparticles. At high Co loading, most of the Co is reduced, forming monometallic Co NPs with little unreduced Co^{II}.

3.3. Synchrotron X-ray Powder Diffraction. Due to the small sizes of the bimetallic NPs, the resulting peaks are broad and low in intensity and high-flux synchrotron radiation is required. The high X-ray energy (105.70 keV or $\lambda = 0.1173$ Å) gives diffraction patterns at lower 2θ angles in comparison to the laboratory XRD, typically from 0 to 10°.

Figure 8A shows the XRD pattern for the $3Pt/SiO_2$ catalyst. Due to the small size of these NPs, the peaks are broader than those for the bulk metallic Pt fcc structure, but it is clear that all of the reflections match those of the simulation. Therefore, this catalyst contains fully reduced monometallic fcc Pt. On the basis of the peak intensity, the size of the nanoparticle was determined as 2.5 nm through the Scherrer equation, consistent with the STEM.

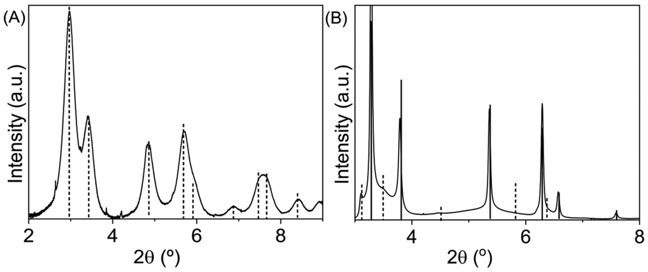

Figure 8. XRD patterns for (A) $3Pt/SiO_2$ (solid line) with metallic Pt peak positions identified (vertical dotted lines) and (B) $10Co/SiO_2$ (solid lines), with peaks identified for fcc Co (vertical solid lines) and hcp Co (vertical dotted lines).

The XRD pattern for $10Co/SiO_2$ is shown in Figure 8B. In this pattern, two different phases can be identified on the basis of the peak positions: hcp and fcc Co. The fcc peaks in the catalysts are very sharp and narrow, suggesting the presence of large nanoparticles. The peaks corresponding to the hcp structure are broader and represent a stacking fault in the crystallites. The XRD patterns for all catalysts were measured at room temperature after reduction in H_2 at 550 °C to reduce the effects of thermal displacement of the peaks at high temperatures. At room temperature, metallic Co has an hcp structure and, as the temperature increases, it converts to fcc. Upon cooling the structure reverts back to hcp. However, as Figure 8B shows, if cooling occurs rapidly, the fcc structure does not fully relax to the hcp structure. Therefore, some Co is present in the hcp structure, while the majority remains in the fcc structure. The estimated particle size calculated from the Scherrer equation was 12 nm, which is consistent with the TEM particle size determination.

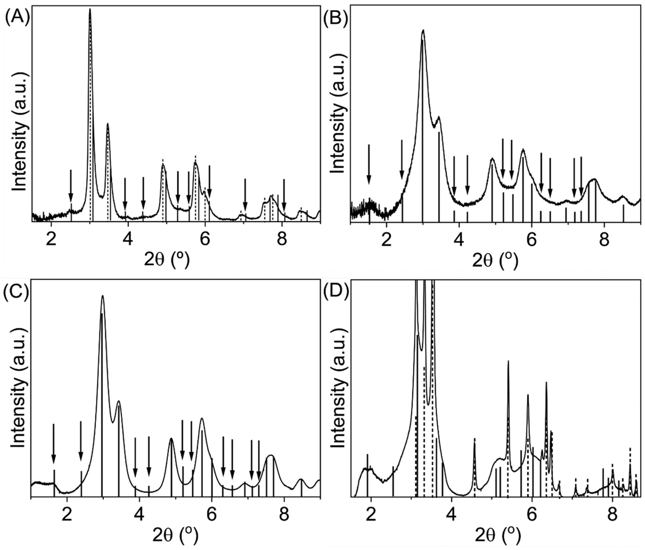

Figure 9. XRD patterns for (A) $2Pt0.6Co/SiO_2$ in comparison to the Pt fcc pattern (dotted vertical line) with lattice parameter *a* contracted by 0.5% ($\Delta a = -0.5\%$) and Pt_3Co alloy phase (solid vertical lines) with $\Delta a = -1.5\%$, (B) 2Pt1Co nanoparticles in comparison to the Pt_3Co alloy phase (solid vertical line) with $\Delta a = -0.5\%$ and superlattice peaks indicated by arrows, (C) 2Pt2Co nanoparticles in comparison to the Pt_3Co alloy phase (solid vertical line) with $\Delta a = -0.5\%$ and superlattice peaks indicated by arrows, (D) for 2Pt4Co nanoparticles in comparison to Co hcp (dotted vertical line) and orderd PtCo alloy phase (solid vertical lines) with $\Delta a = -1.0\%$ and 1.5% contraction for lattice parameter *c*.

Figure 9A shows the diffraction pattern for the 2Pt0.6Co catalyst. In this catalyst, all peaks are slightly asymmetric toward higher 2θ angles. This asymmetric shape is the result of overlapping peaks of two different, but closely related, phases. A comparison to simulated patterns reveals that the peaks are consistent with monometallic Pt and Pt_3Co intermetallic alloy. The large peak positions are similar to those of fcc Pt, while the shoulders represent the peaks from the Pt_3Co alloy phase. However, both Pt and Pt_3Co are slightly shifted to higher 2θ angles in comparison to bulk structures. This occurs due to the small size and the contraction of the bond distance in the NPs, resulting in surface strain effects and slightly smaller lattice parameters. Thus, the simulations were adjusted for lattice parameter contractions. These (Figure 9A) have the lattice parameter, *a*, contracted by 0.5% for the Pt phase and 1.5% for the Pt_3Co (structure type Au_3Cu), corresponding to 0.014 and

0.041 Å, respectively. These changes are consistent with the shorter bond distances in the EXAFS spectra.

In addition to the asymmetric peaks, superlattice peaks arising from the lower symmetry of Pt_3Co are observed in the diffraction pattern. Since these nanoparticles are less than 2 nm in size, these peaks are very small, as shown in Figure 9A. The superlattice positions are given in Table 4. Thus, the XRD pattern indicates the presence of two phases in 2Pt0.6Co: monometallic Pt and Pt_3Co.

Table 4. Peak Positions Identified for the Ordered Alloy Phases in Each Catalyst Diffraction Pattern

catalyst	phase	main XRD diffraction peaks (deg)	XRD superlattice peaks (deg)
2Pt0.6Co	Pt3Co	3.03, 3.5, 4.96, 5.81, 6.07, 7.01, 7.64, 7.84	2.48, 3.92, 4.30, 5.26, 5.54, 6.32, 6.56, 7.23, 7.44
2Pt1Co	Pt3Co	2.99, 3.45, 4.88, 5.73, 5.98, 6.91, 7.53, 7.72	2.44, 3.86, 4.23, 5.18, 5.46, 6.23, 6.46, 7.12, 7.33, 7.91
2Pt2Co	Pt3Co	2.99, 3.43, 4.87, 5.72, 6.00, 6.91, 7.52, 7.71	2.40, 3.88, 4.25, 5.20, 5.47, 6.30, 6.57, 7.12, 7.29
2Pt4Co	likely PtCo	3.10, 3.54, 5.08, 5.88, 6.03	1.82, 2.50, 3.65, 3.98, 4.43, 5.00, 5.32, 5.48, 5.59, 6.20

Figure 9A shows the diffraction pattern for the $2Pt1Co/SiO_2$ catalyst. The peaks are symmetrical and broad. In comparison with the simulated pattern, a good agreement was obtained for the Pt_3Co phase with a 0.5% contraction in the lattice parameter a. Weak superlattice peaks are also observed, and their positions are given in Table 4. The 2Pt2Co diffraction pattern (Figure 9C) had very small, broad diffraction peaks with some peaks matching those of Pt_3Co; however, other peaks could not be identified.

The diffraction pattern for $2Pt4Co/SiO_2$ shows significant differences from the previous catalysts (Figure 9D). Two different phases can be identified in these nanoparticles. The first phase contains large, sharp peaks corresponding to a Co hcp pattern (with 1.0% contraction in lattice parameter a and 1.5% contraction in lattice parameter c), suggesting the presence of larger monometallic Co nanoparticles. This agrees with the results from STEM and EXAFS fits. The second phase contains very small and broad peaks, indicating the presence of small bimetallic Pt−Co nanoparticles. However, due to the small size and the interference of much larger Co peaks, it is difficult to confirm the presence of either PtCo or Pt_3Co. Some peaks match closely those of PtCo (between 5 and 6°, Table 4). However, it is difficult to confirm this structure from the remaining peaks.

On the basis of the XRD results, at very low Co loadings, there are two phases present: metallic Pt and a smaller ordered Pt_3Co alloy phase. As the Co loading increases, an ordered Pt_3Co alloy phase is formed. At high Co loading, formation of a more Co-rich PtCo alloy phase is likely and metallic Co nanoparticles are also present.

3.4. Surface Characterization. Despite the presence of similar intermetallic phases in the XRD patterns, i.e. Pt_3Co, the varying (Pt−Co):(Pt−Pt) ratios in the FT magnitude EXAFS at the Pt L_{III} edge and the presence of two phases in some of the XRD patterns suggest that the average compositions of the nanoparticles among the catalysts are not similar. It is possible this difference is due to different compositions between the particle interior and the catalytic surface. Due to their small particle size, these catalysts have a large enough surface area that differences in the surface monolayer could be detected by EXAFS. Therefore, to characterize the surface structure, oxidation experiments were performed, and the oxidized and reduced spectra were subtracted to obtain the difference spectra corresponding to the surface composition (see the Experimental Section for details).

3.4.1. Pt L_{III} Edge—Oxidized Sample: Core Structure. After H_2 reduction at 550 °C, the catalysts were exposed at room temperature to flowing 20% O_2 (balance He). Upon oxidation, there are losses of surface Pt−Pt and Pt−Co metallic bonds. The remaining metallic bonds in the spectra (Pt−Co and Pt−Pt), therefore, are due to metallic atoms from the nanoparticle interior: i.e., the NP core. Since there is a large fraction of surface atoms in these small NPs, by a comparison of the ratios of (Pt−Co):(Pt−Pt) bonds between the fully reduced and oxidized particles, it is possible to evaluate whether the composition is homogeneous throughout the particle. In addition, the ratio of Pt−Co to Pt−Pt neighbors can be used to identify the ordered surface structure. Table 5 summarizes the fitting results from the k^2-weighted Fourier transform (FT) of the EXAFS spectra at the Pt L_{III} edge for the oxidized bimetallic catalysts.

The oxidation of 2Pt1Co led to a CN of 1.3 Pt−O bonds at 2.05 Å, 2.3 Pt−Pt bonds at 2.73 Å and 1.2 Pt−Co bonds at 2.56 Å. Fully oxidized Pt has 4 Pt−O bonds (at 2.05 Å). Thus, the fraction of oxidized Pt, i.e., surface atoms, is given by the Pt−O CN/4. The (Pt−Co):(Pt−Pt) CN ratio of the metallic core is 0.51, similar to that of the fully reduced 2Pt1Co (ca. 0.5) (Table 2). Thus, the core and average compositions are very similar.

The oxidation of 2Pt2Co led to a CN of 1.3 Pt−O bonds at 2.05 Å, and the metallic bonds in the core were a good fit for 1.3 CN for Pt−Pt at 2.69 Å and a CN of 1.5 Pt−Co for 2.56 Å. The

Table 5. EXAFS Data at the Pt L_{III} Edge for Surface-Oxidized Bimetallic Pt−Co and Monometallic Pt Catalysts

catalyst	edge energy (keV)	bond	bond length (Å)	CN	(Pt−Co):(Pt−Pt)	σ^2	E_0 shift (eV)
2Pt0.6Co	11.5641	Pt−O	2.05	0.5	0.29	0.001	5.44
		Pt−Pt	2.73	7.6		0.002	0.29
		Pt−Co	2.56	2.2		0.002	−3.38
2Pt1Co	11.5645	Pt−O	2.05	1.3	0.52	0.001	0.19
		Pt−Pt	2.73	2.3		0.002	−0.59
		Pt−Co	2.56	1.2		0.002	1.80
2Pt2Co	11.5644	Pt−O	2.05	1.3	1.67	0.001	1.62
		Pt−Pt	2.69	0.9		0.002	0.25
		Pt−Co	2.56	1.5		0.002	3.89
2Pt4Co	11.5645	Pt−O	2.05	1.2	2.23	0.001	1.24
		Pt−Pt	2.69	1.7		0.002	−2.54
		Pt−Co	2.56	3.8		0.002	5.54

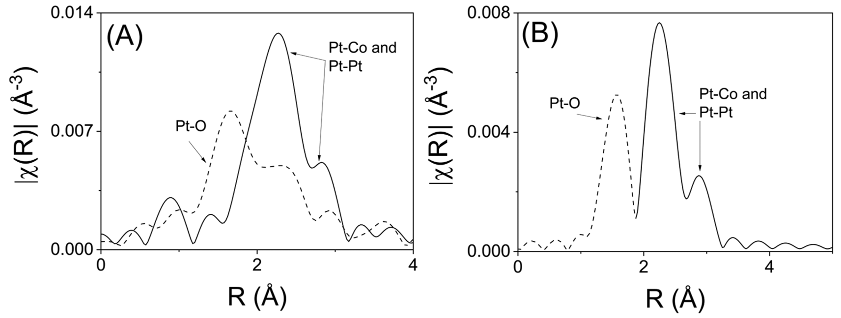

Figure 10. FT magnitude of the EXAFS spectra for 2Pt1Co at the Pt L_{III} edge: (A) both oxidized (dashed line) and fully reduced catalysts (solid line); (B) magnitude of the FT of the difference EXAFS spectra with Pt−O peaks (dashed line) and metallic peaks (solid line).

(Pt−Co):(Pt−Pt) CN ratio in the reduced sample is 0.97, while the metallic peaks in the core (oxidized catalyst) have a ratio of 1.7. This significant difference suggests a nonuniform metallic distribution, with the core composition much richer in Co than in the fully reduced NP.

The oxidized 2Pt4Co catalyst had 1.2 Pt−O bonds at 2.05 Å, 1.7 Pt−Pt bonds at 2.69 Å, and 3.8 Pt−Co bonds at 2.56 Å. The (Pt−Co):(Pt−Pt) CN ratio is 2.2, similar to that of 2.1 in the reduced catalyst (Table 2), suggesting a generally uniform metal distribution throughout the NPs.

3.4.2. Pt L_{III} Edge—Difference Spectra: Surface Structure. The difference in the EXAFS spectra of reduced and room temperature oxidized catalysts represents the surface composition, since the core atoms remain unchanged and are subtracted from the two spectra. These reduced, oxidized, and difference spectra are shown in Figure 10. In Figure 10a, the large peaks (solid line) of the reduced catalysts represent both Pt−Pt and Pt−Co bonds from 2 to 3 Å. The dotted line in Figure 10A shows the oxidized spectrum with loss of metallic neighbors and addition of a Pt−O peak at about 1.5 Å (phase uncorrected distance). In these bimetallic Pt−Co catalysts, the fraction of surface atoms is high; thus, there is a significant Pt−O peak, which can be fit. However, in larger particles greater than about 10 nm the smaller number of Pt−O bonds often overlap the larger metal peaks in the oxidized sample and are difficult to accurately fit. In the difference spectrum, any atoms that are unchanged are not present. Thus, the Pt−Pt, Pt−Co, and Pt−O peaks are more easily resolved and fit in the difference EXAFS spectrum (Figure 10B). The fits for the difference EXAFS spectra are shown in Table 6.

An unexpected result in Table 6 is that the (Pt−Co):(Pt−Pt) CN ratio is 0.5 for all catalysts, despite the clear difference in their average and core compositions. This suggests that all catalysts likely have the same surface structure with different core compositions.

3.5. Catalyst Performance Testing. To further characterize the surface, the bimetallic catalysts were tested for their propane dehydrogenation. A comparison between the catalytic surface of the bimetallic particles and that of their monometallic catalyst counterparts, i.e. Pt and Co, allows the identification of the exposed metals on the surface of the bimetallic catalysts.

Catalytic dehydrogenation of propane to propylene was conducted under two different conditions: without and with H_2 cofeeding at 550 °C. The latter provides a more severe test of catalyst performance than the former.

Table 6. Fitting Results for the Fourier Transform Magnitude for the Difference Spectra at the Pt L_{III} Edge for the Bimetallic Pt−Co and Monometallic Pt Catalysts

catalyst	bond	bond length (Å)	CN	(Pt−Co):(Pt−Pt)	σ^2	E_0 shift (eV)
3Pt	Pt−O	2.05	0.9		0.001	−1.10
	Pt−Pt	2.77	2.5		0.002	0.00
2Pt0.6Co	Pt−O	2.05	0.2	0.5	0.001	0.31
	Pt−Pt	2.73	0.6		0.002	−0.25
	Pt−Co	2.56	0.3		0.002	6.41
2Pt1Co	Pt−O	2.05	0.9	0.5	0.001	−4.62
	Pt−Pt	2.73	2.1		0.002	1.32
	Pt−Co	2.56	1.0		0.002	−3.64
2Pt2Co	Pt−O	2.05	0.9	0.5	0.001	−1.77
	Pt−Pt	2.73	2.4		0.002	−2.35
	Pt−Co	2.56	1.2		0.002	3.02
2Pt4Co	Pt−O	2.05	0.7	0.5	0.001	−2.16
	Pt−Pt	2.73	1.9		0.002	−3.14
	Pt−Co	2.56	0.9		0.002	2.53

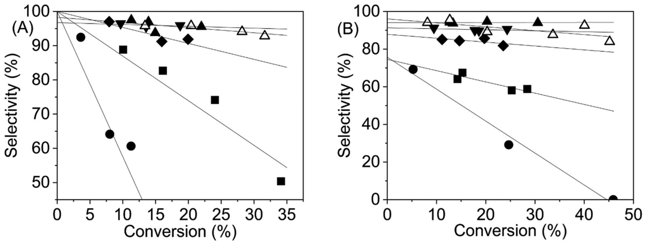

Figure 11. Conversion vs selectivity at 550 °C and atmospheric pressure: (A) without H_2 at a total flow rate of 200 cm^3/min, 2.5% C_3H_8; (B) in the presence of H_2, total flow rate of 250 ccm^3/min, 2% C_3H_8 and 1% H_2. Catalysts evaluated: 3Pt (filled squares), 10Co (filled circles), 2Pt0.6Co (filled upward triangles), 2Pt1Co (filled downward triangles), 2Pt2Co (unfilled upward triangles) and 2Pt4Co (filled tilted squares).

The experimental results in the absence of H_2 are shown in Figure 11A. Each data point corresponds to the selectivity and conversion from a separate catalyst test. For each test the catalysts were tested over a period of 30 min and the conversion and selectivity were extrapolated to zero time and minimal deactivation, which is plotted in Figure 12. The space velocity was varied (at constant temperature) to achieve different propane conversions from 5% to about 40%.

For the monometallic catalysts, there is a very sharp decrease in selectivity as the conversion increases. For monometallic Pt (without H_2), the selectivity is around 88% at 10% conversion, which decreases to about 72% at 25% conversion. For the monometallic Co, the selectivity is even lower, about 60% at 10% conversion. The activity of the Co NPs was low, and it was difficult to obtain much higher conversions at 550 °C. The single-site catalyst Co^{II}/SiO_2 was also tested at the same

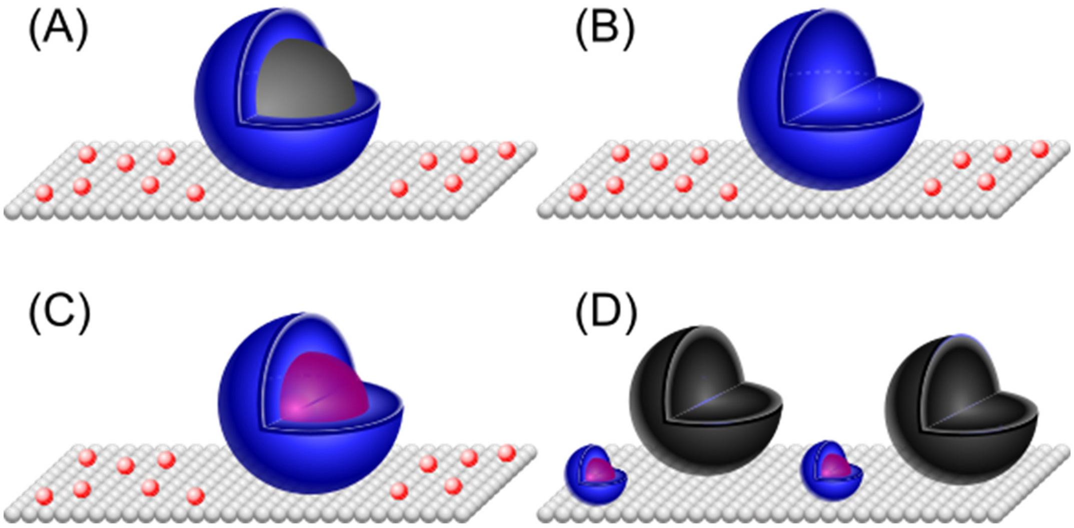

Figure 12. Schematics of the evolution of alloy formation as the Co loading increases: (A) 2Pt0.6Co, Pt_3Co alloy surface (blue) with a Pt core (gray); (B) 2Pt1Co, full Pt_3Co alloy (blue sphere); (C) 2Pt2Co, Pt_3Co alloy surface (blue) with a PtCo alloy core (purple); (D) 2Pt4Co, same bimetallic particles as for 2Pt2Co and large monometallic Co nanoparticles. The excess Co^{II} single sites are represented as red spheres in (A)−(C).

temperature and space velocity, but the obtained conversions were negligible under these conditions. Due to its low activity, 2% Co^{II}/SiO_2 requires significantly more catalyst and lower flow rates of C_3H_8 to reach 5% conversion, where the selectivity was high at 99%. Therefore, in the Pt−Co bimetallic catalysts the contribution from single-site catalysts is negligible at the tested temperature and space velocities.

The bimetallic Pt−Co samples, on the other hand, showed a very different trend in comparison to monometallic Pt and Co. As the conversion increases, all of the bimetallic samples showed a slight decrease in the selectivity. The 2Pt0.6Co catalyst maintained a constant selectivity at 96% from 10% to 25% conversion. Both 2Pt1Co and 2Pt2Co catalyst, from 10% to 20% conversion, had a selectivity similar to that of 2Pt0.6Co, at 96% selectivity. Despite the large fraction of metallic Co in 2Pt4Co, this catalyst also had a constant selectivity of around 92% from 10% to 20% conversion.

Since hydrogen (H_2) is required for hydrogenolysis, cofeeding H_2 is a more severe test of propylene selectivity. A second set of experiments was performed with 1.25% H_2 and 2.5% C_3H_8 (1:2 ratio). The conversions versus selectivities at zero time on stream of monometallic and bimetallic catalysts are shown in Figure 11B.

With addition of H_2, Pt catalysts display a significant decrease in the selectivity in comparison to that in no H_2. As the conversion increases, the selectivity loss is less rapid than that in the absence of H_2. At high conversions, the olefin selectivity is very similar to that without H_2, about 60% at 30% conversion.

The propylene selectivity of 2Pt0.6Co decreased much less than that observed for Pt, and this selectivity remained nearly constant at 94% (in comparison to 96% without H_2) with increasing conversion, a behavior similar to the experiments in the absence of H_2. Both 2Pt1Co and 2Pt2Co had a slightly lower selectivity in comparison to 2Pt0.6Co, but their selectivity also remained constant at about 90% with increasing conversions from 7% to 25%. The $2Pt4Co/SiO_2$ catalyst had the lowest selectivity of these bimetallic catalysts. In the presence of H_2, the selectivity decreased to 85% from 10% to 25% conversion, in comparison to 92% without H_2.

Table 7 summarizes the propylene selectivity at 20% conversion for these catalysts in the absence and presence of H_2. The yields for the remaining products (methane, ethane, and ethylene) are also given. Although both monometallic Pt and Co display low propylene selectivity, all bimetallic Pt−Co catalysts have significantly improved olefin selectivity, generally greater than about 95% in the absence of H_2. This similar selectivity suggests that the catalytic surface is similar in all lower loadings of Co (0.6−2%): i.e., Pt_3Co. The slightly lower selectivity in 2Pt4Co suggests that excess Co in the bimetallic NPs has a slightly negative effect on the selectivity, which is likely due to the presence of monometallic Co nanoparticles and Co-rich core. Under the more severe testing conditions, i.e. in the presence of H_2, the propylene selectivity affects the catalysts differently: the slight decrease in selectivity as the loading increases suggest that the excess Co might have a slight negative effect on selectivity under harsher conditions, despite the same surface composition. This effect might be due to either adsorption of H_2 on the neighboring Co atoms or the subsurface composition of the nanoparticles. The effect of the subsurface composition on the olefin selectivity has recently been reported,

Table 7. Propylene Selectivity at Zero Deactivation Time at 20% Conversion of Propane

	without H_2 feeding[a]		with H_2 cofeeding[b]	
sample	$CH_4/C_2H_6/C_2H_4$ yield (%)	propylene selectivity (%)	$CH_4/C_2H_6/C_2H_4$ yield (%)	propylene selectivity (%)
2Pt0.6Co	1.1/0.4/2.5	96	1.2/0.9/3.3	94
2Pt1Co	0.6/0.5/2.9	96	2.4/2.6/4.5	90
2Pt2Co	0.6/0.4/3	96	2.4/3.3/5.3	89
2Pt4Co	3/0.4/4.6	92	5.8/2/7.2	85
3Pt	17/1/5	77	28/2/8	62
10Co	61/0/20	19	47/0/13	40

[a] No H_2 cofeed in the inlet. Reaction conditions: 550 °C, atmospheric pressure, total flow rate 200 cm^3/min, 2.0% C_3H_8 and balance N_2. [b] H_2 was cofed in the inlet stream. Reaction conditions: 550 °C, atmospheric pressure,total flow rate 250 cm^3/min, 2.0% C_3H_8, 1.0% H_2 (2:1 ratio) and balance N_2.

where different selectivities were achieved on the basis of the subsurface layer composition.[27]

3.5.1. Turnover Rate (TOR) Determination. For a reliable comparison of catalytic rates and identification of the active metal, it is necessary to normalize the conversion by the number of active sites: i.e., a turnover rate (TOR). In these catalysts, both Pt and Co are potentially the active atoms. Therefore, it is necessary to normalize the rate on the basis of the surface composition of each metal. While a common method for determination of the fraction of surface atoms is chemisorption, this method is not effective for quantification of active Co and Pt, since both metals may adsorb CO. To overcome this problem, the previously shown difference EXAFS spectra can be used to quantify the surface fraction of each metal.

Since fully oxidized Pt has 4 Pt−O bonds (at 2.05 Å), the Pt dispersion can be calculated by dividing the Pt−O CN (the difference spectra in Table 6) by 4. The fraction of surface Co atoms was calculated to be half that of the Pt dispersion, since each catalyst appears to have a surface composition of Pt_3Co with a (Pt−Co):(Pt−Pt) ratio of 1:2. Table 8 summarizes the Pt dispersion and TORs calculated for each catalyst for both the surface Pt and surface Co. For 10% Co/SiO_2, the dispersion was calculated on the basis of the nominal dispersion from the XRD and STEM particle size determination.

Table 8. Summary of Dispersion Obtained from EXAFS Difference Spectra

		TOR per surface	
catalyst	fraction of surface Pt[a]	Pt ($mol_{C_3H_8}\ mol_{Pt}^{-1}\ s^{-1}$)[b]	Co ($mol_{C_3H_8}\ mol_{Co}^{-1}\ s^{-1}$)[c]
$3Pt/SiO_2$	0.23	0.2	
$10Co/SiO_2$			0.1×10^{-1} [d]
$2Pt0.6Co/SiO_2$	0.08	0.8	1.6
$2Pt1Co/SiO_2$	0.23	0.9	2.4
$2Pt2Co/SiO_2$	0.23	0.9	1.8
$2Pt4Co/SiO_2$	0.18	0.4	0.7

[a] The fraction of surface Pt was calculated on the basis of the ratio between the CN for Pt−O from the difference spectra and the CN of 4 for Pt−O in the reference used. [b] TOR for both bimetallic and monometallic Pt was based on the number of Pt atoms exposed on the surface, obtained from the surface Pt in the previous column. [c] TOR for the bimetallic Pt−Co catalysts was based on the exposed Co atoms on the surface. This was obtained from the 1:2 ratio of P(t−Co):(Pt−Pt) bonds on the Pt_3Co alloy. [d] Surface Co atoms for the monometallic catalyst was based on the nominal dispersion from the average particle size from STEM, i.e. 0.08 fraction of surface Co.

As shown in Table 8, the TOR for monometallic Co is much lower than that of monometallic Pt: i.e., 1.0×10^{-2} and 2.0×10^{-1}, respectively. The TORs for the bimetallic catalysts based on Pt are similar in all catalysts and similar to that of monometallic Pt. On the other hand, the TORs based on (bimetallic) Co are much higher than that of monometallic Co. Thus, the TORs suggest that Pt is the active site for propane dehydrogenation and Co contributes little to the observed conversion.

4. DISCUSSION

4.1. Alloy Formation. According to the Pt−Co phase diagram,[28] there are two ordered intermetallic structures for binary alloys (Figure 1): Pt_3Co and PtCo with Au_3Cu and AuCu structure types, respectively. The catalysts in this study show not only the presence of both structures but also the evolution of their formation with increasing Co loading.

Pt is reduced at a much lower temperature (250 °C) than for Co (750 °C). Thus, it is likely that small Pt nanoparticles are initially formed. The addition of Co leads to bimetallic Pt−Co at a temperature lower than that required for Co reduction, suggesting that Pt catalyzes the reduction of Co, likely near the Pt NP. The catalyzed reduction of Co leads to small bimetallic NPs of size similar to that of the initially formed monometallic Pt. At low cobalt loadings, i.e. 2Pt0.6Co, there are two phases: fcc Pt and Pt_3Co (Au_3Cu structure type). The difference EXAFS spectra and catalytic performance indicate that the surface is Pt_3Co (Figure 1B), while the metal peaks of the oxidized sample indicate a Pt-rich interior. The XANES spectra at the Co K edge indicate the presence of both Co^0 and Co^{II} oxidation states, about 0.41 Co^{II} single sites and 0.59 Co^0 associated with the bimetallic particles. Recent calculations by Saedy et al.[39] showed that Co atoms easily diffuse into Pt NPs and spread evenly among the Pt layers, maximizing the Pt around Co interaction and preferentially forming Pt_3Co. The fcc-like structure minimizes the energy required for rearrangement from the Pt fcc structure. Although there is sufficient Co in 2Pt0.6Co for a full Pt_3Co alloy, the formation of a stable surface Pt_3Co on the Pt-rich core also indicates that the Co atoms do not diffuse to the NP interior until there is additional Co near the NP surface. The unreduced Co^{2+} in the catalysts, therefore, is likely away from the bimetallic NPs.

As the Co loading increases, for example in the 2Pt1Co catalyst, a full Pt_3Co alloy is formed. The NP composition is confirmed by XRD. The EXAFS spectrum of the reduced particle (Table 2) and difference (Table 5) EXAFS spectrum of the surface have (Pt−Co):(Pt−Pt) CN ratios of around 0.5, consistent with a bulk and surface of Pt_3Co.[40−43] The Co K-edge XANES spectrum indicates there are both Co^{II} and Co^0, 0.89 and 0.11, respectively (Table 3). Thus, since the excess Co is not reduced at 550 °C, the Co^{II} ions are likely distant from the bimetallic NPs.

Further increases in Co loading, e.g., 2Pt2Co, produce bimetallic NPs with a (Pt−Co):(Pt−Pt) CN ratio of about 1, which indicates the presence of more Co than is required for the Pt_3Co structure. While Pt_3Co has a (Pt−Co):(Pt−Pt) CN ratio of 0.5, the PtCo alloy (Figure 1a) has 8 Pt−Co bonds at 2.6 Å, 4 Pt−Pt bonds at 2.69 Å, and a (Pt−Co):(Pt−Pt) CN ratio of 2. Thus, 2Pt2Co is likely a mixture of these two phases. While the average (Pt−Co):(Pt−Pt) CN ratio is 1, the surface CN ratio is about 0.5, consistent with Pt_3Co. The metallic core has a (Pt−Co):(Pt−Pt) CN ratio of 1.7, consistent with a large fraction of PtCo. The Co K edge is a mixture of Co^{II}, about 0.79, and 0.21 Co^0 (or 0.4% Co). Full formation of PtCo would require 0.6 g of Co for a full PtCo alloy. Thus, the fraction of metallic Co from the XANES spectrum is also consistent with a mixture of Pt_3Co and PtCo. The XRD pattern for this catalyst contains peaks consistent with Pt_3Co; however, these are weak and other peaks are also present, which does not allow for precise determination of the structure(s). Thus, the XRD pattern supports a Pt_3Co phase but is inconclusive for the presence of a PtCo alloy phase. Nevertheless, the EXAFS spectrum indicates that in 2Pt2Co the

NPs are more Co rich than in 2Pt1Co, for example. Thus, despite the similarity in the surface structures, the core is likely a large fraction of PtCo alloy. The presence of Co^{II} in this catalyst again indicates that the majority of the Co is distant from the bimetallic NPs and is dispersed on the support.

At the highest loading, 2Pt4Co, the EXAFS spectrum indicates a (Pt−Co):(Pt−Pt) ratio of 2.23, very similar to that of a PtCo structure. The NP core has a (Pt−Co):(Pt−Pt) CN ratio near 2, consistent with PtCo alloy at the NP interior. However, the difference spectrum of the surface has a 0.5 ratio, suggesting a Pt_3Co structure, similar to the case for the other catalysts. The XRD pattern, however, is inconclusive for the identification of these two phases, due to the very small, broad peaks of the bimetallic particles and the interference of large Co NP peaks. Although the Pt_3Co on the surface cannot be confirmed by XRD, this diffraction pattern does show two phases: Co hcp structure, with sharp peaks, and broad peaks of PtCo, with a AuCu structure type. In this catalyst, nearly all of the Co is reduced to metallic NPs, as in either the PtCo alloy or monometallic Co. Nevertheless, the excess Co, which forms large monometallic NPs, does not lead to enrichment of the Pt_3Co surface. Thus, it is possible Pt_3Co is a more thermodynamically stable phase.

The summary of these characterizations leads to the structures and morphologies shown in Figure 12. The specific NP composition, structure, and morphology depend on the Pt:Co ratio and the availability of Co near the Pt NPs, which are initially formed. While the exact structure and morphology are different at different Co loadings, the surface of each is a Pt_3Co structure.

4.2. Geometric Effect of Pt_3Co on Propylene Selectivity. On the basis of the TOR shown in Table 8, monometallic Co has a TOR about 20 times lower than that of monometallic Pt. The TORs based on the Pt atoms on the surface of the bimetallic Pt−Co catalysts have values similar to that of monometallic Pt. The similarity in TOR and the difference between the TORs of monometallic Pt and Co suggest that Co activity is negligible in comparison to that of Pt and propane molecules preferentially react on Pt sites. Therefore, despite monometallic Co catalysts being active, metallic Co behaves as an inactive structural promoter in Pt−Co alloys, similar to Zn, Sn, Ga, In, and other post-transition elements, and Pt atoms behave as the only active site.

In the bulk face-centered cubic (fcc) structure, Pt has 12 other Pt neighbors at a bond distance of 2.77 Å. In the Pt_3Co intermetallic alloy, there is a decrease in the Pt−Pt coordination number to 8 with 4 Pt−Co bonds. Assuming that the surface plane is the most stable with the highest atom density, the Pt−Pt ensembles of the (111) planes in Pt and Pt_3Co are shown in Figure 13. In the monometallic Pt, there are ensembles of more than 7 Pt atoms. In Pt_3Co, however, there are 3-fold Pt−Pt ensembles symmetrically distributed at 2.75 Å.

Since hydrogenolysis is a structure-sensitive reaction, the decrease in the Pt ensemble size significantly inhibits the cleavage of C−C bonds. For example, in the Pt (111) facet, where ensembles of more than 5 Pt atoms are close together, hydrogenolysis is still likely due to adsorption of propane on multiple Pt atoms. The Pt catalyst has a propylene selectivity of 77% at 20% conversion (Table 7). Once a Pt_3Co surface is formed, the large Pt ensembles are broken, and the new ensembles have 3 adjacent Pt atoms on a (111) facet. Propane now has fewer Pt sites and hydrogenolysis is inhibited. This leads to a decrease in the rate of the structure-sensitive hydrogenolysis, while it has little effect on the rate of the structure-insensitive dehydrogenation reaction.[44,45] Propylene selectivity increases to 96% at the same conversion (Table 7). The suppression of hydrogenolysis by structural changes on the surface leads to an increased propylene selectivity, similar to geometric effects for nonactive promoter atoms reported for Pt_3M and PtM intermetallic alloys with Sn, Zn, In, Mn, and Cu.[17,18,26,27,46]

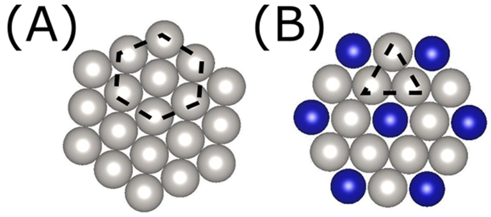

Figure 13. Possible exposed planes and their respective Pt ensemble size (dashed black line) for each structure: (A) Pt (111); (B), Pt3Co (111). Pt atoms are shown in gray and Co atoms in blue.

In the absence of cofed H_2, the selectivities are similar in all Pt−Co catalysts despite the increased Co loading, due to the same Pt_3Co surface in all catalysts. As the Co content of the bimetallic NPs increases, there is a slight but continual decrease in the olefin selectivity in the presence of cofed H_2, suggesting that the core composition affects the selectivity. As the Co in the core increases, there is a slight decrease in the olefin selectivity.

4.3. Electronic Effects of Alloying. As observed in Figure 4, the formation of bimetallic Pt−Co particles affects the XANES spectra, resulting in a slightly lower intensity of the white line and an edge shift toward higher energies. Since the XANES spectra result from a dipole-allowed photoexcitation of a 2p electron and an unfilled Pt 5d orbital, these changes suggest an increase in the energy of the unfilled d orbitals. Thus, bonding of Co with Pt changes the energy of the valence orbitals responsible for catalysis. Resonant inelastic X-ray spectra of a Pt_1Zn_1 intermetallic showed that, when the energy of the unfilled orbitals increases, there is a similar decrease in the energy of the filled 5d orbitals, which are responsible for catalysis.[26] The energy of the XANES spectra also increases with increasing Co loading. In order to determine the shift in energy responsible for catalysis, one needs to determine the structure of the surface and also prepare a phase-pure sample of this surface structure. For example, in 2Pt0.6Co, the surface is Pt_3Co, but the XANES spectrum is characterized by the sum of all Pt atoms. Since there are two phases, Pt_3Co and Pt, the XANES energy shift is not characteristic of the surface. For this sample the XANES energy is too low. Similarly, for 2Pt4Co, there are also two phases, Pt_3Co and PtCo. Again, the surface is Pt_3Co, but the XANES energy is too large and is not representative of the surface. Only in the 2Pt1Co is there a single phase where the NP and surface compositions are the same. Thus, the XANES spectrum of this sample correctly reflects the electronic changes in the surface Pt atoms. Other methods for characterization of the electronic properties, for example XPS or RIXS, would be similarly affected. Proper quantification of the changes in the electronic properties of the surface are also important for DFT modeling of the proper catalytic structure.

The XANES shift to higher energies in Pt_3Co also suggests a lowering of the energy of the filled 5d orbitals. Since the filled Pt 5d orbitals form bonds with reactants, the resulting metal−adsorbate bonds are weaker. These weaker bonds result in lower surface coverage of reactants and products, including propylene and hydrogen. Facile desorption of propylene would also lead to fewer side reactions, such as hydrogenolysis and coking. A lower surface coverage of H_2 would also lead to lower hydrogenolysis rates and improved olefin selectivity. Similar conclusions from theory[27,39,47] and experiment[27] have been reported for other alloy dehydrogenation catalysts.

5. CONCLUSION

Bimetallic catalysts with two active metals, Pt and Co, were synthesized with different Co loadings for propane dehydrogenation. Using in situ XAS, XRD, and an XAS surface analysis, the catalysts were shown to lead to different intermetallic structures with different morphologies related to their Co loading. At low Co loadings, stable surface Pt_3Co surface alloys with a Pt-rich core were formed. As the Co content increased, the catalyst composition formed a full Pt_3Co phase with the excess excess Co^{II} remaining on the silica. Further increases in Co lead to a PtCo alloy phase in the core, despite the surface remaining as Pt_3Co. At high Co loadings, the Co in excess of that needed for bimetallic alloy formation resulted in large monometallic Co nanoparticles. Despite the different nanostructures in these catalysts, the catalytic surface in each of these catalysts had a Pt_3Co structure.

All Pt−Co catalysts have much higher propylene selectivity for propane dehydrogenation in comparison to monometallic Pt or Co. The high selectivity was maintained at high conversion and in the presence of cofed H_2. The TOR of Pt in the bimetallic catalysts is similar to that of monometallic Pt and is suggested to be the active site in these alloys. The catalytic performance of bimetallic Pt−Co is typical of other intermetallic Pt alloys with noncatalytic post-transition elements such as Sn, Zn, Ga, and In. The ability of Co to act as a nonactive promoter is likely due to its lower TOR in comparison to Pt. The high olefin selectivity of the surface Pt_3Co is suggested to be due to geometric effects, where there are smaller Pt−Pt ensembles, as well as a decrease in the energy of the Pt 5d orbitals in comparison to that in monometallic Pt. Therefore, if the activities between two metals are significantly different, i.e. by 1 order of magnitude, the least active metal will likely behave as a noncatalytic promoter, allowing the geometric effects to enhance the selectivity.

Quantification of the surface structure was only possible due to the analysis of the difference EXAFS spectrum of the reduced and oxidized catalysts. The changes in the surface were generally too small to detect by the average EXAFS or XRD of the reduced sample. Identification of a specific structure by EXAFS is generally not possible. However, utilization of XRD to confirm possible nanostructures where the EXAFS can also be obtained allows one to identify the structure from ratios of CNs. Determination of the surface structure is essential for determination of correct structural and electronic effects affecting the catalytic performance. Proper identification of the surface structure along with preparation of NPs with the same uniform structure will allow for proper determination of the geometric and electronic properties, which control the catalytic performance.

AUTHOR INFORMATION

Corresponding Authors

*E-mail for G.Z.: gzhang@dlut.edu.cn.
*E-mail for J.T.M.: mill1194@purdue.edu.

ORCID

Laryssa Goncalves Cesar: 0000-0001-7499-4579
Guanghui Zhang: 0000-0002-5854-6909
Jeffrey T. Miller: 0000-0002-6269-0620

Notes

The authors declare no competing financial interest.

ACKNOWLEDGMENTS

L.G.C. was supported by the scholarship program Ciências sem Fronteiras (Science without Borders), funded by the Brazilian governmental organization Conselho Nacional de Pesquisa (CNPq) in partnership with Laspau, under process no 222473/2014. G.Z. and J.T.M. were supported in part by the National Science Foundation under Cooperative Agreement No. EEC-1647722. G.Z. also wishes to acknowledge the Fundamental Research Funds for the Central Universities (DUT18RC(3)057). Use of the Advanced Photon Source was supported by the U.S. Department of Energy, Office of Basic Energy Sciences, under contract no. DE-AC02-06CH11357. MRCAT operations, beamline 10-BM, are supported by the Department of Energy and the MRCAT member institutions. The authors also acknowledge the use of beamline 11-ID-C at APS.

REFERENCES

(1) Sinfelt, J. H. Catalytic Specificity. *AIChE J.* **1973**, *19*, 673−683.

(2) Cortright, R. D.; Dumesic, J. A. Effects of Potassium on Silica-Supported Pt and Pt/Sn Catalysts for Isobutane Dehydrogenation. *J. Catal.* **1995**, *157*, 576−583.

(3) Sun, P.; Siddiqi, G.; Vining, W. C.; Chi, M.; Bell, A. T. Novel Pt/Mg(In)(Al)O Catalysts for Ethane and Propane Dehydrogenation. *J. Catal.* **2011**, *282*, 165−174.

(4) Zhang, Y.; Zhou, Y.; Qiu, A.; Wang, Y.; Xu, Y.; Wu, P. Propane Dehydrogenation on PtSn/ZSM-5 Catalyst: Effect of Tin as a Promoter. *Catal. Commun.* **2006**, *7*, 860−866.

(5) Pham, H. N.; Sattler, J. J. H. B.; Weckhuysen, B. M.; Datye, A. K. Role of Sn in the Regeneration of Pt/γ-Al_2O_3 Light Alkane Dehydrogenation Catalysts. *ACS Catal.* **2016**, *6*, 2257−2264.

(6) Zangeneh, F. T.; Sahebdelfar, S.; Bahmani, M. Propane Dehydrogenation over a Commercial Pt-Sn/Al_2O_3 Catalyst for Isobutane Dehydrogenation: Optimization of Reaction Conditions. *Chin. J. Chem. Eng.* **2013**, *21*, 730−735.

(7) Zangeneh, F. T.; Mehrazma, S.; Sahebdelfar, S. The Influence of Solvent on the Performance of Pt-Sn/θ-Al_2O_3 Propane Dehydrogenation Catalyst Prepared by Co-Impregnation Method. *Fuel Process. Technol.* **2013**, *109*, 118−123.

(8) Zangeneh, F. T.; Taeb, A.; Gholivand, K.; Sahebdelfar, S. Kinetic Study of Propane Dehydrogenation and Catalyst Deactivation over Pt-Sn/Al_2O_3 Catalyst. *J. Energy Chem.* **2013**, *22*, 726−732.

(9) Fan, X.; Li, J.; Zhao, Z.; Wei, Y.; Liu, J.; Duan, A.; Jiang, G. Dehydrogenation of Propane over PtSn/SBA-15 Catalysts: Effect of the Amount of Metal Loading and State. *RSC Adv.* **2015**, *5*, 28305−28315.

(10) Barias, O. A.; Holmen, A.; Blekkan, E. a. Propane Dehydrogenation over Supported Pt and Pt-Sn Catalysts: Catalyst Preparation, Characterization, and Activity Measurements. *J. Catal.* **1996**, *158*, 1−12.

(11) Gómez-Quero, S.; Tsoufis, T.; Rudolf, P.; Makkee, M.; Kapteijn, F.; Rothenberg, G. Kinetics of Propane Dehydrogenation over Pt-Sn/Al_2O_3. *Catal. Sci. Technol.* **2013**, *3*, 962−971.

(12) Gallagher, J. R.; Childers, D. J.; Zhao, H.; Winans, R. E.; Meyer, R. J.; Miller, J. T. Structural Evolution of an Intermetallic Pd−Zn Catalyst Selective for Propane Dehydrogenation. *Phys. Chem. Chem. Phys.* **2015**, *17*, 28144−28153.

(13) Collins, S.; Baltanas, M.; Garciafierro, J.; Bonivardi, A. Gallium−Hydrogen Bond Formation on Gallium and Gallium−Palladium Silica-Supported Catalysts. *J. Catal.* **2002**, *211*, 252−264.

(14) Siddiqi, G.; Sun, P.; Galvita, V.; Bell, A. T. Catalyst Performance of Novel Pt/Mg(Ga)(Al)O Catalysts for Alkane Dehydrogenation. *J. Catal.* **2010**, *274*, 200−206.

(15) Ballarini, A. D.; Zgolicz, P.; Vilella, I. M. J.; de Miguel, S. R.; Castro, A. A.; Scelza, O. A. N-Butane Dehydrogenation on Pt, PtSn and PtGe Supported on γ-Al_2O_3 Deposited on Spheres of α-Al_2O_3 by Washcoating. *Appl. Catal., A* **2010**, *381*, 83−91.

(16) Bocanegra, S. A.; Scelza, O. A.; De Miguel, S. R. Behavior of PtPb/MgAl2O4 Catalysts with Different Pb Contents and Trimetallic PtPbIn Catalysts in n-Butane Dehydrogenation. *Appl. Catal., A* **2013**, *468*, 135−142.

(17) Ma, Z.; Wu, Z.; Miller, J. T. Effect of Cu Content on the Bimetallic Pt-Cu Catalysts for Propane Dehydrogenation. *Catal. Struct. React.* **2017**, *3*, 43−53.

(18) Wegener, E. C.; Wu, Z.; Tseng, H. T.; Gallagher, J. R.; Ren, Y.; Diaz, R. E.; Ribeiro, F. H.; Miller, J. T. Structure and Reactivity of Pt−In Intermetallic Alloy Nanoparticles: Highly Selective Catalysts for Ethane Dehydrogenation. *Catal. Today* **2018**, *299*, 146−153.

(19) Wu, Z.; Wegener, E. C.; Tseng, H.-T.; Gallagher, J. R.; Harris, J. W.; Diaz, R. E.; Ren, Y.; Ribeiro, F. H.; Miller, J. T. Pd−In Intermetallic Alloy Nanoparticles: Highly Selective Ethane Dehydrogenation Catalysts. *Catal. Sci. Technol.* **2016**, *6*, 6965−6976.

(20) Ye, C.; Wu, Z.; Liu, W.; Ren, Y.; Zhang, G.; Miller, J. T. Structure Determination of a Surface Tetragonal Pt1Sb1Phase on Pt Nanoparticles. *Chem. Mater.* **2018**, *30*, 4503−4507.

(21) Boudart, M.; Aldag, A.; Benson, J. E.; Dougharty, N. A.; Harkins, C. G. On the Specific Activity of Platinum Catalysts. *J. Catal.* **1966**, *6*, 92−99.

(22) Boudart, M. Catalysis by Supported Metals. *Adv. Catal.* **1969**, *20*, 153−166.

(23) Pines, H.; Manassen, J. The Mechanism of Dehydration of Alcohols over Alumina Catalysts. *Adv. Catal.* **1966**, *16*, 49−93.

(24) Che, M.; Bennett, C. O. The Influence of Particle Size on the Catalytic Properties of Supported Metals. *Adv. Catal.* **1989**, *36*, 55−172.

(25) Clarke, J. K. A.; Rooney, J. J. Stereochemical Approaches to Mechanisms of Hydrocarbon Reactions on Metal Catalysts. *Adv. Catal.* **1976**, *25*, 125−183.

(26) Cybulskis, V. J.; Bukowski, B. C.; Tseng, H.-T.; Gallagher, J. R.; Wu, Z.; Wegener, E.; Kropf, A. J.; Ravel, B.; Ribeiro, F. H.; Greeley, J.; Miller, J. T. Zinc Promotion of Platinum for Catalytic Light Alkane Dehydrogenation: Insights into Geometric and Electronic Effects. *ACS Catal.* **2017**, *7*, 4173−4181.

(27) Wu, Z.; Bukowski, B. C.; Li, Z.; Milligan, C.; Zhou, L.; Ma, T.; Wu, Y.; Ren, Y.; Ribeiro, F. H.; Delgass, W. N.; Greeley, J.; Zhang, G.; Miller, J. T. Changes in Catalytic and Adsorptive Properties of 2 Nm Pt3Mn Nanoparticles by Subsurface Atoms. *J. Am. Chem. Soc.* **2018**, *140*, 14870−14877.

(28) Okamoto, H. Co-Pt (Cobalt-Platinum). *J. Phase Equilib.* **2001**, *22*, 591−591.

(29) Du, N.; Wang, C.; Long, R.; Xiong, Y. N-Doped Carbon-Stabilized PtCo Nanoparticles Derived from Pt@ZIF-67: Highly Active and Durable Catalysts for Oxygen Reduction Reaction. *Nano Res.* **2017**, *10*, 3228−3237.

(30) Song, C.; Zhang, D.; Wang, B.; Cai, Z.; Yan, P.; Sun, Y.; Ye, K.; Cao, D.; Cheng, K.; Wang, G. Uniformly Grown PtCo-Modified Co_3O_4 Nanosheets as a Highly Efficient Catalyst for Sodium Borohydride Electrooxidation. *Nano Res.* **2016**, *9*, 3322−3333.

(31) Mehrabadi, B. A. T.; Eskandari, S.; Khan, U.; White, R. D.; Regalbuto, J. R. A Review of Preparation Methods for Supported Metal Catalysts. *Adv. Catal.* **2017**, *61*, 1−35.

(32) Hu, B.; Bean Getsoian, A.; Schweitzer, N. M.; Das, U.; Kim, H.; Niklas, J.; Poluektov, O.; Curtiss, L. A.; Stair, P. C.; Miller, J. T.; Hock, A. S. Selective Propane Dehydrogenation with Single-Site Co^{II} on SiO_2 by a Non-Redox Mechanism. *J. Catal.* **2015**, *322*, 24−37.

(33) Schneider, C. A.; Rasband, W. S.; Eliceiri, K. W. NIH Image to ImageJ: 25 Years of Image Analysis. *Nat. Methods* **2012**, *9*, 671−675.

(34) Ressler, T. WinXAS: A Program for X-Ray Absorption Spectroscopy Data Analysis under MS-Windows. *J. Synchrotron Radiat.* **1998**, *5*, 118−122.

(35) Ravel, B.; Newville, M. ATHENA, ARTEMIS, HEPHAESTUS: Data Analysis for X-Ray Absorption Spectroscopy Using IFEFFIT. *J. Synchrotron Radiat.* **2005**, *12*, 537−541.

(36) Hammersley, A. P.; Svensson, S. O.; Hanfland, M.; Fitch, A. N.; Häusermann, D. Two-Dimensional Detector Software: From Real Detector to Idealised Image or Two-Theta Scan. *High Press. Res.* **1996**, *14*, 235−248.

(37) Lutterotti, L.; Chateigner, D.; Ferrari, S.; Ricote, J. Texture, Residual Stress and Structural Analysis of Thin Films Using a Combined X-Ray Analysis. *Thin Solid Films* **2004**, *450*, 34−41.

(38) Miller, J. T.; Kropf, A. J.; Zha, Y.; Regalbuto, J. R.; Delannoy, L.; Louis, C.; Bus, E.; van Bokhoven, J. A. The Effect of Gold Particle Size on Au-Au Bond Length and Reactivity toward Oxygen in Supported Catalysts. *J. Catal.* **2006**, *240*, 222−234.

(39) Saedy, S.; Palagin, D.; Safonova, O.; van Bokhoven, J. A.; Khodadadi, A. A.; Mortazavi, Y. Understanding the Mechanism of Synthesis of Pt3Co Intermetallic Nanoparticles via Preferential Chemical Vapor Deposition. *J. Mater. Chem. A* **2017**, *5*, 24396−24406.

(40) Woolley, J. C.; Phillips, J. H.; Clark, J. A. Ordering in CoPt-CrPt and CoPt-MnPt Alloys. *J. Less-Common Met.* **1964**, *6*, 461−471.

(41) Raub, E. Metals and Alloys of the Platinum Group. *J. Less-Common Met.* **1959**, *1*, 3−18.

(42) Buschow, K. H. J.; van Engen, P. G.; Jogenbreur, R. Magneto-Optical Properties of Metallic Ferromagnetic Materials. *J. Magn. Magn. Mater.* **1983**, *38*, 1−22.

(43) Jen, S. U. Effect of Atomic Order on Some Physical Properties of $Co_{25}Pt_{75}$. *J. Alloys Compd.* **1996**, *234*, 231−234.

(44) Chambers, R. P.; Boudart, M. Lack of Dependence of Conversion on Flow Rate in Catalytic Studies. *J. Catal.* **1966**, *6*, 141−145.

(45) Boudart, M. Turnover Rates in Heterogeneous Catalysis. *Chem. Rev.* **1995**, *95*, 661−666.

(46) Galvita, V.; Siddiqi, G.; Sun, P.; Bell, A. T. Ethane Dehydrogenation on Pt/Mg(Al)O and PtSn/Mg(Al)O Catalysts. *J. Catal.* **2010**, *271*, 209−219.

(47) Nykänen, L.; Honkala, K. Density Functional Theory Study on Propane and Propene Adsorption on Pt(111) and PtSn Alloy Surfaces. *J. Phys. Chem. C* **2011**, *115*, 9578−9586.